CrossMark

Influence of transition metal element (Co, Ni, Cu) doping on structural, electrical and magnetic properties of $Bi_{0.9}Ca_{0.1}FeO_3$ nanoparticles

Chuye Quan[1] · Zhengfei Qin[1] · Yiyi Zhu[1] · Zhongchao Wang[1] · Jian Zhang[1] · Weiwei Mao[1,2] · Xingfu Wang[1,2] · Jianping Yang[2] · Xing'ao Li[1] · Wei Huang[1,3]

Abstract The multiferroic $Bi_{0.9}Ca_{0.1}FeO_3$, $Bi_{0.9}Ca_{0.1}Fe_{0.9}Co_{0.1}O_3$, $Bi_{0.9}Ca_{0.1}Fe_{0.9}Ni_{0.1}O_3$, $Bi_{0.9}Ca_{0.1}Fe_{0.9}Cu_{0.1}O_3$ samples were prepared by a simple sol–gel method. Rietveld refinement of X-ray diffraction data and Raman spectra reflect a structural phase transition from single phase (rhombohedral, pure $BiFeO_3$) to two phase coexistence (rhombohedral R3c and cubic Fm-3 m). The structural distortion of $Bi_{0.9}Ca_{0.1}Fe_{0.9}Ni_{0.1}O_3$ is very marked. SEM images show the co-doped nanoparticles having an average size of 50 nm. A contribution from the leakage current have been observed in the P–E loops. XPS results reveal that the concentration of Fe^{2+} and oxygen vacancy decreased after transition metal elements (Co, Ni, Cu) doped into $Bi_{0.9}Ca_{0.1}FeO_3$. Moreover Co, Ni doping can enhance the saturation magnetization, while Cu doping can enhance the coercive field in $Bi_{0.9}Ca_{0.1}FeO_3$.

Chuye Quan and Zhengfei Qin have contributed equally to this work.

✉ Xing'ao Li
   lxahbmy@126.com

✉ Wei Huang
   iamwhuang@njupt.edu.cn.com

1 Key Laboratory for Organic Electronics and Information Displays (KLOEID), Synergetic Innovation Center for Organic Electronics and Information Displays (SICOEID), Institute of Advanced Materials (IAM), School of Materials Science and Engineering (SMSE), Nanjing University of Posts and Telecommunications (NUPT), Nanjing 210023, People's Republic of China

2 School of Science, Nanjing University of Posts and Telecommunications (NUPT), Nanjing 210023, People's Republic of China

3 Key Laboratory of Flexible Electronics (KLOFE) and Institute of Advanced Materials (IAM), National Synergistic Innovation Center for Advanced Materials (SICAM), Nanjing Tech University (Nanjing Tech), 30 South Puzhu Road, Nanjing 211816, China

1 Introduction

Multiferroic materials are currently attracting intensive studies interests due to the potential applications for developing novel storage media and spintronics devices [1–4]. The multiferroic materials could coupled with electric, magnetic, and structural order parameters which result in simultaneous ferroelectricity, ferromagnetism, and/or ferroelasticity [5]. $BiFeO_3$ (BFO) is the most outstanding multiferroic inorganic compound among the currently research, because its ferroelectric Curie point ($T_C = 1103$ K) and antiferromagnetic Néel point ($T_N = 643$ K) are both above room temperature (RT) [6]. However, the net spins are canceled and the macroscopic magnetization is averaged to zero due to the cycloid spin modulation with a period of about 62 nm in BFO, which restrict multiferroic properties [7].

Recently, numerous investigations have focused on substitution of rare-earth, alkaline earth or transition metal elements at A-site (Ba [8], Ca [9], Eu [10], Nd [11], La [12]), B-site (Mn [13], Co [14], Ni [15], Cu [16], Zn [17]) or A–B-site [18–21] of BFO to improve its multiferroic. Additionally the overall properties of BFO depend on numerous factors including structure, defect, size, and morphology, which can also be promoted by this strategy. Our previous works focus on alkali metal element Ca. It is worthy noticing that the Ca-doped structure has half-metallic characteristic and enhanced ferromagnetism [22]. The study of Ca co-doped with rare earth element Nd in BFO have been published recently, in which we gain a relatively low current leakage density and an enhanced

ferromagnetic properties [23]. As we known Fe-site substitution by $3d$ transition metal ions might induce structure modifications to suppress the cycloidal spin structure and the ferromagnetic interaction between Fe and $3d$ transition metal ions which might further enhance the room temperature ferromagnetism [24]. We would further investigate on Ca co-doped with $3d$ transition metal elements to recover the influence on the properties of BFO.

In this paper, BFO, $Bi_{0.9}Ca_{0.1}FeO_3$, $Bi_{0.9}Ca_{0.1}Fe_{0.9}Co_{0.1}O_3$, $Bi_{0.9}Ca_{0.1}Fe_{0.9}Ni_{0.1}O_3$ and $Bi_{0.9}Ca_{0.1}Fe_{0.9}Cu_{0.1}O_3$ were prepared via a facile sol–gel method. Detailed studies on structure, electrical and magnetic properties of the samples were investigated.

2 Experimental details

Samples of BFO, $Bi_{0.9}Ca_{0.1}FeO_3$, $Bi_{0.9}Ca_{0.1}Fe_{0.9}Co_{0.1}O_3$, $Bi_{0.9}Ca_{0.1}Fe_{0.9}Ni_{0.1}O_3$ and $Bi_{0.9}Ca_{0.1}Fe_{0.9}Cu_{0.1}O_3$ were prepared by the sol–gel method. High purity Bi_2O_3 (analytical pure), CaO ($\geq$98.5 %), Co_2O_3 ($\geq$98.5 %), NiO ($\geq$98.5 %), CuO ($\geq$98.5 %), $Fe(NO_3)_3 \cdot 9H_2O$ ($\geq$98.5 %) powders were carefully weighed in stoichiometric proportions and thoroughly dissolved in nitric acid and deionized water under constant magnetic stirring. Tartaric acid was added as a chelating agent. All the chemicals in this work were purchased from the Shanghai Chemical Factory of China and were used without further purification. The mixed solution was dry at 110 °C for 4 h to form a homogeneous gel. The gel was then dried at 80 °C for 48 h and calcined at 600 °C for 2 h.

The phase identification was examined for the samples by X-ray diffractometer (XRD) (Bruker D8 Advance X-ray diffractometer) with Cu Ka radiation. Structure simulation based on XRD patterns were obtained by using Rietveld crystal structure refinement software (FullProf). The surface morphology was examined by scanning electron microscope (SEM: S4800). Raman measurements were carried out on Labram HR800 Raman microscope ($\lambda = 514$ nm) at room temperature. In order to measure the ferroelectric hysteresis loops and leakage current, the nanoparticles were pressed to pellets and sintered under 500 °C. The dielectric properties were measured by using Radiant precision materials analyzer. The combination states of Fe $2p$ electron in the samples were examined by X-ray photoelectron spectroscopy (XPS) (ESCALAB 250Xi). The magnetic hysteresis loops were measured at room temperature by Vibrating sample magnetometer (SQUID).

3 Results and discussion

Figure 1 shows XRD patterns of Co, Ni, Cu-substituted $Bi_{0.9}Ca_{0.1}FeO_3$ nanoparticles. The symbol "*" indicates the impurity phases of Bi_2O_3. Impurity peak is restrained

after doping. The occurrence of impurity peaks is due to the volatile nature of Bi in the pure BFO sample, which can be weakened after Ca^{2+} substitute of Bi^{3+}. For pure BFO all diffraction peaks are well matched with the rhombohedrally distorted perovskite structure with R3c space group (JCPDS no. 71-2494). It is obvious that the (104) and (110) peaks merge into one broad peak in $Bi_{0.9}Ca_{0.1}FeO_3$ $Bi_{0.9}Ca_{0.1}Fe_{0.9}Co_{0.1}O_3$, $Bi_{0.9}Ca_{0.1}Fe_{0.9}Ni_{0.1}O_3$ and $Bi_{0.9}Ca_{0.1}Fe_{0.9}Cu_{0.1}O_3$ compared to the pure BFO sample, which indicate structural phase transition. The merged peaks were shifted to a lower 2θ angle direction, which may not affected by ionic radius ($R_{Ca2+} < R_{Bi3+}$). For more detailed study of structural transformation, Rietveld's whole-profile fitting were performed using FullProf software. Fitting parameters are listed in Table 1 and Table 2. It is noticed that the pure BFO confirms a single-phase (rhombohedral structure), while the doped samples show the state of two-phase coexistence. In detail, the rate of rhombohedral phase (R3c:H space group), in $Bi_{0.9}Ca_{0.1}FeO_3$, $Bi_{0.9}Ca_{0.1}Fe_{0.9}Co_{0.1}O_3$, $Bi_{0.9}Ca_{0.1}Fe_{0.9}Ni_{0.1}O_3$ and $Bi_{0.9}Ca_{0.1}Fe_{0.9}Cu_{0.1}O_3$ nanoparticles, dominates about 91.77, 18.21, 17.8 and 92.17 % respectively. The second phase is cubic Fm-3 m for all the doped samples. Unit cell volume of $Bi_{0.9}Ca_{0.1}Fe_{0.9}Ni_{0.1}O_3$ changed apparently compared with other samples, as can be seen in Table 1, which means the structural distortion of $Bi_{0.9}Ca_{0.1}Fe_{0.9}Ni_{0.1}O_3$ is very seriously. From Table 2 we can see that the estimated bond length of Fe–O bond decreased after doping, which implies the distortion in the magnetic Fe^{3+} position decreases with dopant and the opening/straightening of the canted spin.

In order to show the structural distortion intuitively, we draw the unit cell structures of all samples by Diamond software, as shown in Fig. 2. The Fe atom has slightly drifted from the center of the FeO_6 octahedral for
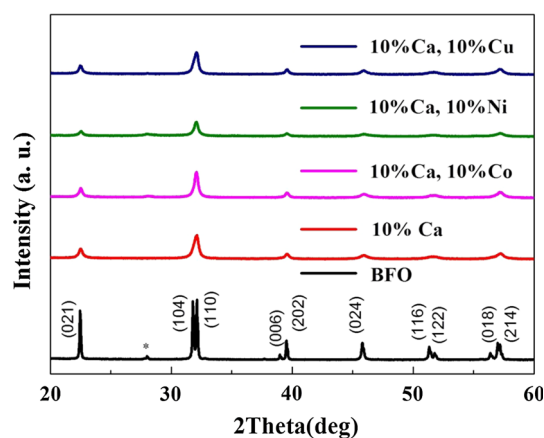

Fig. 1 Evolution of X-ray diffraction data of $BiFeO_3$, $Bi_{0.9}Ca_{0.1}FeO_3$, $Bi_{0.9}Ca_{0.1}Fe_{0.9}Co_{0.1}O_3$, $Bi_{0.9}Ca_{0.1}Fe_{0.9}Ni_{0.1}O_3$ and $Bi_{0.9}Ca_{0.1}Fe_{0.9}Cu_{0.1}O_3$ nanoparticles

Table 1 The refined crystal structure parameters and profile R-factors of BFO, $Bi_{0.9}Ca_{0.1}FeO_3$, $Bi_{0.9}Ca_{0.1}Fe_{0.9}Co_{0.1}O_3$, $Bi_{0.9}Ca_{0.1}Fe_{0.9}Ni_{0.1}O_3$ and $Bi_{0.9}Ca_{0.1}Fe_{0.9}Cu_{0.1}O_3$ nanoparticles

Sample	Cell type	Cell (Å)	R factors (%)	Bragg R-factor	RF-factor	GoF-index
BFO	R3c	a = 5.5790	Rp = 12.3	1.19	1.15	1.4
		b = 5.5790	Rwp = 10.9			
		c = 13.8705	Re = 7.59			
		V = 373.89	χ^2 = 2.050			
10 %Ca	R3c (91.77 %)	a = 5.5873	Rp = 16.7	2.04	1.47	1.4
		b = 5.5873	Rwp = 14.6			
		c = 13.7904	Re = 10.4			
		V = 372.833	χ^2 = 1.967			
	Fm-3 m (8.23 %)	a = 7.8990		8.11	3.15	
		b = 7.8990				
		c = 7.8990				
		V = 492.843				
10 %Ca, 10 %Co	R3c (18.21 %)	a = 5.5831	Rp = 15.8	1.43	1.25	1.3
		b = 5.5831	Rwp = 13.5			
		c = 13.7581	Re = 10.4			
		V = 371.40	χ^2 = 1.689			
	Fm-3 m (81.79 %)	a = 7.8875		0.951	1.22	
		b = 7.8875				
		c = 7.8875				
		V = 490.70				
10 %Ca, 10 %Ni	R3c (17.80 %)	a = 5.5890	Rp = 21.3	1.99	0.956	1.2
		b = 5.5890	Rwp = 17.5			
		c = 13.8848	Re = 15.1			
		V = 375.61	χ^2 = 1.352			
	Fm-3 m (82.20 %)	a = 7.9028		1.17	0.877	
		b = 7.9028				
		c = 7.9028				
		V = 493.56				
10 %Ca, 10 %Cu	R3c (92.17 %)	a = 5.5806	Rp = 15.9	1.25	0.916	1.2
		b = 5.5806	Rwp = 13.1			
		c = 13.8339	Re = 11.2			
		V = 373.12	χ^2 = 1.378			
	Fm-3 m (7.83 %)	a = 7.8984		0.829	0.696	
		b = 7.8984				
		c = 7.8984				
		V = 492.74				

Table 2 The bond length and bond angle for the BFO, $Bi_{0.9}Ca_{0.1}FeO_3$, $Bi_{0.9}Ca_{0.1}Fe_{0.9}Co_{0.1}O_3$, $Bi_{0.9}Ca_{0.1}Fe_{0.9}Ni_{0.1}O_3$ and $Bi_{0.9}Ca_{0.1}Fe_{0.9}Cu_{0.1}O_3$ compounds obtained by Rietveld refinement of the XRD patterns at room temperature

Sample	BFO	10 % Ca		10 % Ca, 10 % Co		10 % Ca, 5 % Ni		10 % Ca, 5 % Cu	
Cell type	R3c	R3c	Fm-3 m	R3c	Fm-3 m	R3c	Fm-3 m	R3c	Fm-3 m
Bi–O bond distance (Å)	2.5464/ 2.2863	2.7687/ 2.1315	2.7991/ 2.7991	2.7103/ 2.1842	2.7886	2.5800/ 1.8581	2.7941	2.4920/ 2.2435	2.7925
Average Bi–O bond distance (Å)	2.41613	2.4501	2.7991	2.4473	2.7886	2.219	2.7941	2.3678	2.7925
Fe–O bond distance (Å)	1.9583/ 2.0886	1.7555/ 1.7555	1.9793/ 1.9793	1.9785/ 2.0490	1.9719	1.8947	1.9757	1.7996/ 2.3306	1.9746
Average Fe–O bond distance (Å)	2.0235	1.7555	1.9793	2.0137	1.9719	1.8947	1.9757	2.0651	1.9746
Fe–O–Fe (°)	156.614	157.125	180.000	158.351	180.000	125.246	180.000	146.901	180.000

$Bi_{0.9}Ca_{0.1}FeO_3$, $Bi_{0.9}Ca_{0.1}Fe_{0.9}Co_{0.1}O_3$ and $Bi_{0.9}Ca_{0.1}Fe_{0.9}Cu_{0.1}O_3$. However the structural transformation evident than the other samples.

Figure 3 shows the SEM images of the co-doped samples. The average size of the co-doped samples are about 50 nm, smaller than 62 nm, which may lead to the destroy of cycloidal spiral structure. Hence, the magnetism can be enhanced. A certain degree of agglomeration of crystal particle can be observed in the co-doped samples.
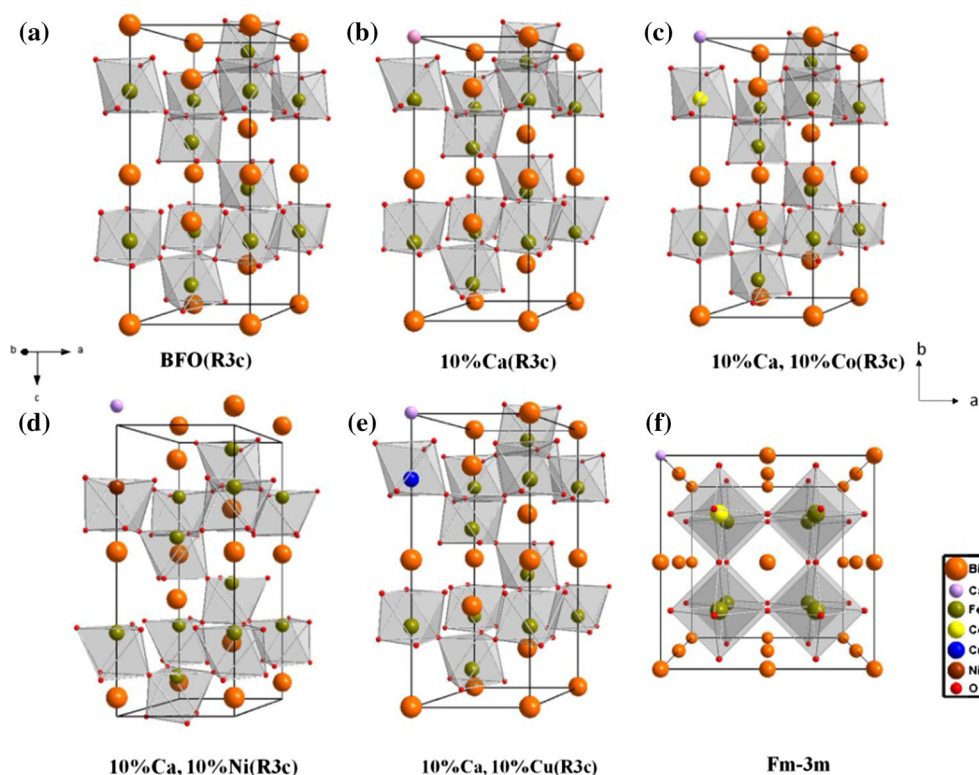
Figure 4 shows the Raman scattering spectra of BFO, $Bi_{0.9}Ca_{0.1}FeO_3$, $Bi_{0.9}Ca_{0.1}Fe_{0.9}Co_{0.1}O_3$, $Bi_{0.9}Ca_{0.1}Fe_{0.9}Ni_{0.1}O_3$ and $Bi_{0.9}Ca_{0.1}Fe_{0.9}Cu_{0.1}O_3$ samples. According to the group theoretical calculation, there are 27 ($13A' + 14A''$), 13 ($4A_1 + 9E$), and 8 ($3A_1 + B_1 + 4E$) distinct Raman active modes for BFO with monoclinic (M), rhombohedral (R), and tetragonal (T) structure, respectively [25]. All of the major active modes that appeared in the pure BFO are matched well with those of the rhombohedrally distorted (R3c) perovskite structure. The 13 Raman active modes peaks are located at 141, 167, 215, 267, 275, 302, 343, 369, 467, 520 and 609 cm^{-1} respectively. The low frequency modes have been assigned to the vibration of Bi–O, high frequency Raman modes are related to the stretching and bending of Fe–O [26]. The intensity of A_1-2 phonon mode decreased and A_1-1 phonon mode shifts to higher frequency side for doped samples, which could be attributed to the Ca doping, as atomic mass of Ca is less than that of Bi [27]. The phonon modes at high frequency area disappeared or shift to other position which indicate structural distortion after doping. The detailed change of Bi–O and Fe–O bond were shown in Table 2.

Figure 5 shows the polarization hysteresis loops of the $Bi_{0.9}Ca_{0.1}Fe_{0.9}Co_{0.1}O_3$, $Bi_{0.9}Ca_{0.1}Fe_{0.9}Ni_{0.1}O_3$ and $Bi_{0.9}Ca_{0.1}Fe_{0.9}Cu_{0.1}O_3$ nanoparticles under an applied electric field of 10 kV/cm. The values of 2Pr of the $Bi_{0.9}Ca_{0.1}Fe_{0.9}Co_{0.1}O_3$, $Bi_{0.9}Ca_{0.1}Fe_{0.9}Ni_{0.1}O_3$ and $Bi_{0.9}Ca_{0.1}Fe_{0.9}Cu_{0.1}O_3$ nanoparticles are 2.414, 2.537 and 1.535 $\mu C/cm^2$ respectively. The rounded drop-down tips in the P–E loops of $Bi_{0.9}Ca_{0.1}Fe_{0.9}Co_{0.1}O_3$ and $Bi_{0.9}Ca_{0.1}Fe_{0.9}Cu_{0.1}O_3$ is the contribution of the leakage current [28]. The values of 2Ec of the $Bi_{0.9}Ca_{0.1}Fe_{0.9}Co_{0.1}O_3$, $Bi_{0.9}Ca_{0.1}Fe_{0.9}Ni_{0.1}O_3$ and $Bi_{0.9}Ca_{0.1}Fe_{0.9}Cu_{0.1}O_3$ nanoparticles were 0.915, 0.522 and 0.880 kV/mm respectively. Overall, among the transition metal (Co, Ni, Cu) doped $Bi_{0.9}Ca_{0.1}FeO_3$ samples $Bi_{0.9}Ca_{0.1}Fe_{0.9}Co_{0.1}O_3$ showed relative good ferroelectric. However, the leakage current is exist in both of them.

The oxidation state of Fe in $Bi_{0.9}Ca_{0.1}FeO_3$, $Bi_{0.9}Ca_{0.1}Fe_{0.9}Co_{0.1}O_3$, $Bi_{0.9}Ca_{0.1}Fe_{0.9}Ni_{0.1}O_3$ and $Bi_{0.9}Ca_{0.1}Fe_{0.9}Cu_{0.1}O_3$ nanoparticles was investigated by X-ray photoemission spectroscopy (XPS) as shown in Fig. 6. It should be noted that XPS can only analyze surface structure and composition of the materials, due to the limited depth of the beam penetration. The exposed surface might be oxidized by oxygen in the air. However, for BFO and some metallic oxide the effect of oxidation can be neglected [29]. The XPS spectra shows the Fe $2p$ region of the samples,

Fig. 2 A schematic representation of the rhombohedral R3c unit cell and nonpolar cubic Fm-3 m structure, respectively. The distorted Fe–O octahedral are shown in gray
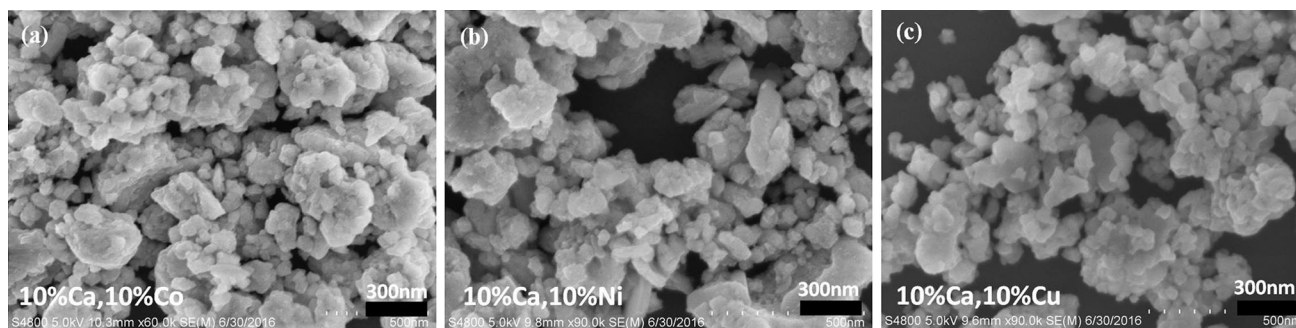
(a) BFO(R3c)
(b) 10%Ca(R3c)
(c) 10%Ca, 10%Co(R3c)
(d) 10%Ca, 10%Ni(R3c)
(e) 10%Ca, 10%Cu(R3c)
(f) Fm-3m

Bi
Ca
Fe
Co
Cu
Ni
O

Fig. 3 SEM images of $Bi_{0.9}Ca_{0.1}Fe_{0.9}Co_{0.1}O_3$, $Bi_{0.9}Ca_{0.1}Fe_{0.9}Ni_{0.1}O_3$ and $Bi_{0.9}Ca_{0.1}Fe_{0.9}Cu_{0.1}O_3$ nanoparticles
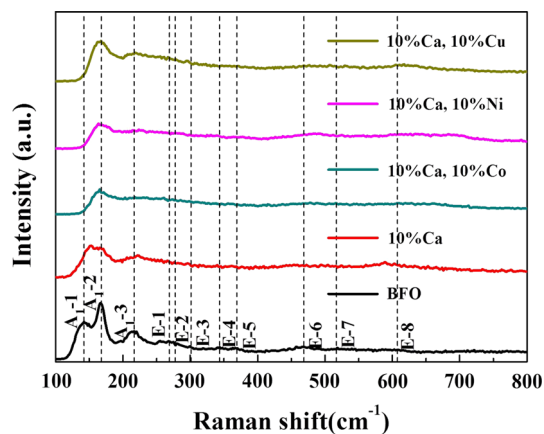
Fig. 4 Measured Raman scattering spectra for $BiFeO_3$, $Bi_{0.9}Ca_{0.1}$ FeO_3, $Bi_{0.9}Ca_{0.1}Fe_{0.9}Co_{0.1}O_3$, $Bi_{0.9}Ca_{0.1}Fe_{0.9}Ni_{0.1}O_3$ and $Bi_{0.9}Ca_{0.1}$ $Fe_{0.9}Cu_{0.1}O_3$ nanoparticles
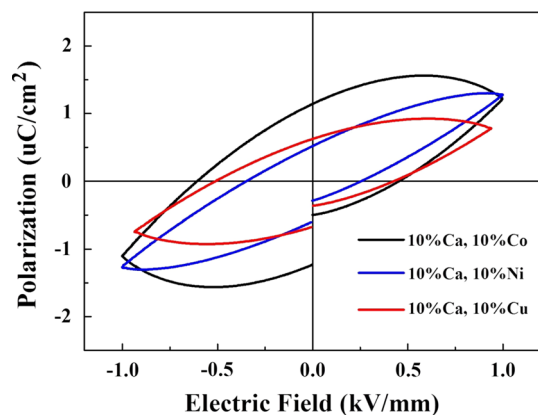
Fig. 5 Polarization versus electrical field loops of $Bi_{0.9}Ca_{0.1}Fe_{0.9}$ $Co_{0.1}O_3$, $Bi_{0.9}Ca_{0.1}Fe_{0.9}Ni_{0.1}O_3$ and $Bi_{0.9}Ca_{0.1}Fe_{0.9}Cu_{0.1}O_3$ nanoparticles at room temperature

where the core level binding energies were aligned with respect to C 1 s peak (284.6 eV). There are two main photoemission peaks around 710 and 724 eV are Fe $2p_{3/2}$ and Fe $2p_{1/2}$, respectively. Fe $2p_{3/2}$ peaks correspond to Fe^{2+} and Fe^{3+}, they show the satellite peak at 6 or 8 eV above their $2p_{3/2}$ principal peaks. The experimental
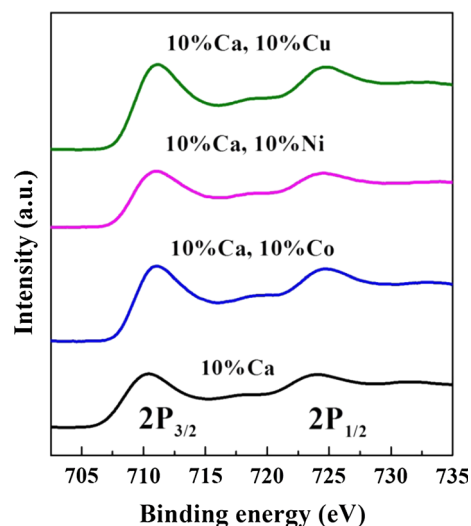
Fig. 6 XPS spectra of the Fe $2p$ lines for $Bi_{0.9}Ca_{0.1}FeO_3$, $Bi_{0.9}Ca_{0.1}$ $Fe_{0.9}Co_{0.1}O_3$, $Bi_{0.9}Ca_{0.1}Fe_{0.9}Ni_{0.1}O_3$ and $Bi_{0.9}Ca_{0.1}Fe_{0.9}Cu_{0.1}O_3$ nanoparticles at room temperature

Fe $2p_{3/2}$ band of all the samples were fitted well by the Gaussian shape, using two peaks corresponding to Fe^{3+} at 710.8 eV and Fe^{2+} at 709.4 eV as shown in Fig. 7.

The ratios of Fe^{3+}/Fe^{2+} determined from the peak areas in the $Bi_{0.9}Ca_{0.1}FeO_3$, $Bi_{0.9}Ca_{0.1}Fe_{0.9}Co_{0.1}O_3$, $Bi_{0.9}Ca_{0.1}$ $Fe_{0.9}Ni_{0.1}O_3$ and $Bi_{0.9}Ca_{0.1}Fe_{0.9}Cu_{0.1}O_3$ nanoparticles are calculated as 1.7:1, 10.1:1, 7.5:1 and 36.4:1 respectively. The results indicate the decrease of Fe^{2+} ions with rare earth element doping into $Bi_{0.9}Ca_{0.1}FeO_3$ nanoparticles. Numerous studies point out that less Fe^{2+} ions imply less oxygen vacancies, which suggest that earth element doping decrease the concentration of oxygen vacancies. In order to prove this, narrow-scan spectra of the O 1 s core levels of $Bi_{0.9}Ca_{0.1}FeO_3$, $Bi_{0.9}Ca_{0.1}Fe_{0.9}Co_{0.1}O_3$, $Bi_{0.9}Ca_{0.1}Fe_{0.9}$ $Ni_{0.1}O_3$ and $Bi_{0.9}Ca_{0.1}Fe_{0.9}Cu_{0.1}O_3$ samples were fitted by Gaussian curve as shown in Fig. 8a–d [30]. All the samples can be fitted by two Gaussians whose peaks positions are 529.05–529.14 eV and 530.79–531.99 eV. The one with lower binding energy can be attributed to the main peak of oxygen atoms, while the other is related to the presence of

Fig. 7 Gaussian fitting results of the Fe $2p_{3/2}$ band for the $Bi_{0.9}Ca_{0.1}FeO_3$, $Bi_{0.9}Ca_{0.1}Fe_{0.9}Co_{0.1}O_3$, $Bi_{0.9}Ca_{0.1}Fe_{0.9}Ni_{0.1}O_3$ and $Bi_{0.9}Ca_{0.1}Fe_{0.9}Cu_{0.1}O_3$ samples

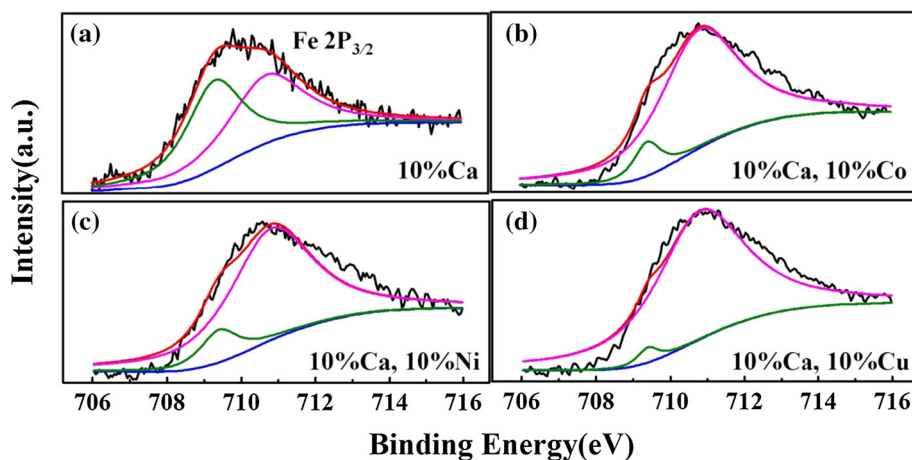**Fig. 8** O 1 s core levels with the Gaussian–Lorentzian dividing peak analysis of $Bi_{0.9}Ca_{0.1}FeO_3$, $Bi_{0.9}Ca_{0.1}Fe_{0.9}Co_{0.1}O_3$, $Bi_{0.9}Ca_{0.1}Fe_{0.9}Ni_{0.1}O_3$ and $Bi_{0.9}Ca_{0.1}Fe_{0.9}Cu_{0.1}O_3$ samples
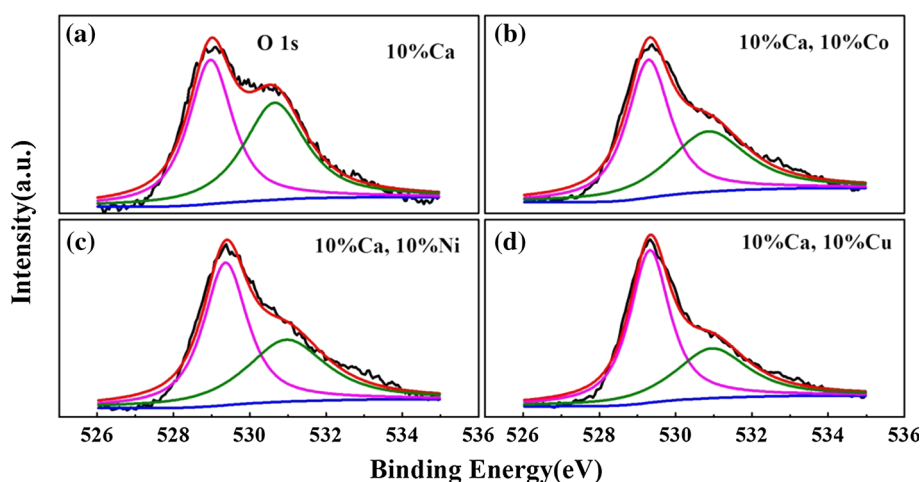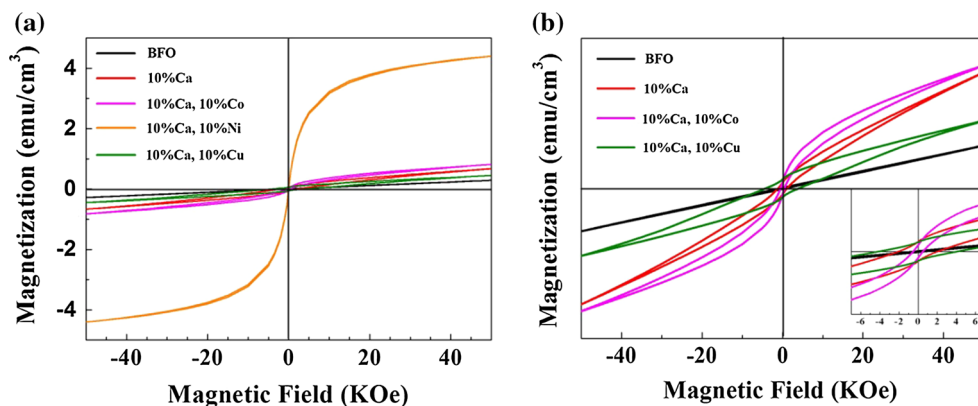

Fig. 9 M–H curves in a magnetic field of 50 KOe at room temperature

oxygen vacancy (V_O). The concentration ratio of V_O and O in $Bi_{0.9}Ca_{0.1}FeO_3$, $Bi_{0.9}Ca_{0.1}Fe_{0.9}Co_{0.1}O_3$, $Bi_{0.9}Ca_{0.1}Fe_{0.9}Ni_{0.1}O_3$ and $Bi_{0.9}Ca_{0.1}Fe_{0.9}Cu_{0.1}O_3$ are 0.94:1, 0.78:1, 0.78:1 and 0.59:1 respectively. It obvious that the concentration of oxygen vacancy in $Bi_{0.9}Ca_{0.1}FeO_3$ is higher than the other three samples, which is in accordance with previous studies.

Figure 9a shows room temperature magnetic hysteresis (M–H) loops of the BFO, $Bi_{0.9}Ca_{0.1}FeO_3$, $Bi_{0.9}Ca_{0.1}Fe_{0.9}Co_{0.1}O_3$, $Bi_{0.9}Ca_{0.1}Fe_{0.9}Ni_{0.1}O_3$ and $Bi_{0.9}Ca_{0.1}Fe_{0.9}Cu_{0.1}O_3$. The saturation magnetization (Ms) of $Bi_{0.9}Ca_{0.1}Fe_{0.9}Ni_{0.1}O_3$ is 99.87 emu/cm^3, which is much larger than the other samples. The big Ms may be attributed to the serious structural distortion. To get better look at the figure, M–H

loops without $Bi_{0.9}Ca_{0.1}Fe_{0.9}Ni_{0.1}O_3$ was shown in Fig. 9b. The existence of Fe^{2+} ions may cause a double exchange interaction between Fe^{2+} and Fe^{3+} ions through oxygen, which can result in the enhancement of ferromagnetism. The XPS spectra analysis shows that the concentration of Fe^{2+} in transition metal (Co, Ni, Cu) doped BFO are smaller than that in Ca-doped BFO. However, the saturation magnetization of $Bi_{0.9}Ca_{0.1}Fe_{0.9}Ni_{0.1}O$ and $Bi_{0.9}Ca_{0.1}Fe_{0.9}Cu_{0.1}O_3$ and the coercive field of $Bi_{0.9}Ca_{0.1}Fe_{0.9}Cu_{0.1}O_3$ is larger than $Bi_{0.9}Ca_{0.1}FeO_3$, which means Fe^{2+}–O–Fe^{3+} interaction is not the main factor that affect the magnetism. The decrease of oxygen vacancies due to doping can result in significant enhancement of saturation magnetization [31]. Structural transformation and size effect may lead to the collapse of the space-modulated spin structure in BFO, which can also enhance the magnetism. Combined action of the reasons mentioned above result in the M–H loops show in Fig. 9.

4 Conclusions

In summary, we have studied the effect of transition metal (Co, Ni, Cu) substitution on $Bi_{0.9}Ca_{0.1}FeO_3$ nanoparticles on its structure, ferroelectricity, leakage current and magnetic property. BFO, $Bi_{0.9}Ca_{0.1}FeO_3$, $Bi_{0.9}Ca_{0.1}Fe_{0.9}Co_{0.1}O_3$, $Bi_{0.9}Ca_{0.1}Fe_{0.9}Ni_{0.1}O_3$ and $Bi_{0.9}Ca_{0.1}Fe_{0.9}Cu_{0.1}O_3$ nanoparticles were successfully synthesized by sol–gel method. Structural phase transition from rhombohedral to two phase coexistence was observed in all the doped BFO. The values of 2Ec of the $Bi_{0.9}Ca_{0.1}Fe_{0.9}Co_{0.1}O_3$, $Bi_{0.9}Ca_{0.1}Fe_{0.9}Ni_{0.1}O_3$ and $Bi_{0.9}Ca_{0.1}Fe_{0.9}Cu_{0.1}O_3$ nanoparticles were 0.915, 0.522 and 0.880 kV/mm respectively. The leakage current exist in transition metal (Co, Ni, Cu) doped $Bi_{0.9}Ca_{0.1}FeO_3$, which is show in the P–E loops. The decrease of oxygen vacancies can increased the saturation magnetization of all the samples. The obvious structural transformation may play an important role in the enhance of saturation magnetization of $Bi_{0.9}Ca_{0.1}Fe_{0.9}Ni_{0.1}O_3$. Fe^{2+}–O–Fe^{3+} interaction and size effect also have an effect on ferromagnetism.

References

1. A.S. Priya, I.B.S. Banu, S. Anwar, Mater. Sci. Eng., B **401**, 333–338 (2016)
2. J.S. Park, Y.J. Yoo, J.S. Hwang, J.H. Kang, B.W. Lee, Y.P. Lee, J. Appl. Phys. **115**, 013904 (2014)
3. G. Cheng, Z.-G. Wang, Y.-L. Liu, J.-L. Zhang, D.-H. Sun, J.-Z. Ni, A.C.S. Appl, Mater. Interfaces **5**, 3182–3190 (2013)
4. G. Cheng, Z.-G. Wang, Y.-L. Liu, J.-L. Zhang, D.-H. Sun, J.-Z. Ni, Chem. Commun. **48**, 10240–10242 (2012)
5. Y.T. Li, Y.W. Fan, H.G. Zhang, X.X. Teng, X.G. Dong, H. Liu, X.P. Ge, Q. Li, W. Chen, X.A. Li, Z.Y. Ge, J. Supercond. Nov. Magn. **27**, 1239–1243 (2014)
6. J.S. Hwang, J.Y. Cho, S.Y. Park, Y.J. Yoo, P.S. Yoo, B.W. Lee, Y.P. Lee, Appl. Phys. Lett. **106**, 062902 (2015)
7. X.J. Xi, S.Y. Wang, W.F. Liu, H.J. Wang, F. Guo, X. Wang, J. Gao, D.J. Li, J. Magn. Magn. Mater. **355**, 259–264 (2014)
8. P. Godara, A. Agarwal, N. Ahlawat, S. Sanghi, K. Kaswan, J. Magn. Magn. Mater. **406**, 76–82 (2016)
9. H.W. Chang, C.Y. Shen, F.T. Yuan, S.H. Tien, S.Y. Lin, W.A. Chen, C.R. Wang, C.S. Tu, S.U. Jen, J. Magn. Magn. Mater. **401**, 673–676 (2016)
10. B.T. El, M. Taibi, A.M. El-Naggar, T.T. Slimani, A.A. Albassam, M. Abd-Lefdil, I.V. Kityk, N.S. AlZayed, A.O. Fedorchuk, J. Mater. Sci.: Mater. Electron. **26**, 9949–9954 (2015)
11. S.M. Lee, A. Cho, Y.S. Cho, RSC Adv. **6**, 16602–16607 (2016)
12. R. Dhanalakshmi, M. Muneeswaran, K. Shalini, N.V. Giridharan, Mater. Lett. **165**, 205–209 (2016)
13. S.K. Singh, H. Ishiwara, K. Sato, K. Maruyama, J. Appl. Phys. **102**, 094109 (2007)
14. J. Wang, M.Y. Li, X.L. Liu, W.Q. Liu, Z.Q. Hu, S.X. Wang, J. Polym. Mater. **20**, 727–731 (2013)
15. S.M. Lee, A. Cho, Y.S. Cho, RSC Adv. **6**, 16602–16607 (2016)
16. Y.T. Li, Y.W. Fan, H.G. Zhang, X.X. Teng, X.G. Dong, H. Liu, X.P. Ge, Q. Li, W. Chen, X.A. Li, J. Supercond Nov. Magn. **27**, 1239–1243 (2014)
17. J.J. Xie, C.D. Feng, X.H. Pan, Y. Liu, Ceram. Int. **40**, 703–706 (2014)
18. J.Y. Chen, Y. Wang, Y. Deng, J. Appl. Phys. **116**, 174102 (2014)
19. X.L. Xu, W.F. Liu, H. Zhang, M.C. Guo, P. Wu, S.Y. Wang, J. Gao, G.H. Rao, J. Appl. Phys. **117**, 174106 (2015)
20. D. Do, J.W. Kim, T.K. Song, S.S. Kim, J. Electroceram. **30**, 55–59 (2013)
21. W.W. Mao, F. Wang, L. Chu, Y.Y. Zhu, Q. Wang, J. Zhang, J.P. Yang, X.A. Li, W. Huang, Phys. Chem. Chem. Phys. **18**, 6399–6405 (2016)
22. C.Y. Quan, Y.M. Han, N. Gao, W.W. Mao, J. Zhang, J.P. Yang, X.A. Li, W. Huang, Ceram. Int. **42**, 537–544 (2016)
23. C.Y. Quan, Y.H. Ma, Y.M. Han, X.X. Tang, M.J. Lu, W.W. Mao, J. Zhang, J.P. Yang, X.A. Li, W. Huang, J. Alloys Comp. **635**, 272–277 (2015)
24. W.W. Mao, X.F. Wang, Y.M. Han, X.A. Li, Y.T. Li, Y.F. Wang, Y.W. Ma, X.M. Feng, T. Yang, J.P. Yang, W. Huang, J. Alloys Comp. **584**, 520–523 (2014)
25. J.-Z. Huang, Y. Shen, M. Li, C.-W. Nan, J. Appl. Phys. **110**, 094106 (2011)
26. J. Zhao, X. Zhang, S. Liu, W. Zhang, Z. Liu, J. Alloys Comp. **557**, 120–123 (2013)
27. P. Kumar, M. Kar, J. Alloys Comp. **584**, 566–572 (2014)
28. Z.Q. Hu, M.Y. Li, Y. Yu, J. Liu, L. Pei, J. Wang, X.L. Liu, B.F. Yu, X.Z. Zhao, Solid State Commun. **150**, 1088–1091 (2010)
29. F. Huang, X. Lu, W. Lin, X. Wu, Y. Kan, J. Zhu, Appl. Phys. Lett. **89**, 242914 (2006)
30. X. Xi, S. Wang, W. Liu, H. Wang, F. Guo, X. Wang, J. Gao, D. Li, J. Magn. Magn. Mater. **355**, 259–264 (2014)
31. G.S. Arya, R.K. Kotnala, N.S. Negi, J. Nanopart. Res. **16**, 2155 (2013)